Journal of Biomedical Optics

SPIEDigitalLibrary.org/jbo

Optical imaging of mitochondrial redox state in rodent model of retinitis pigmentosa

Sepideh Maleki
Sandeep Gopalakrishnan
Zahra Ghanian
Reyhaneh Sepehr
Heather Schmitt
Janis Eells
Mahsa Ranji

SPIE

Optical imaging of mitochondrial redox state in rodent model of retinitis pigmentosa

Sepideh Maleki,[a*] Sandeep Gopalakrishnan,[b*] Zahra Ghanian,[a] Reyhaneh Sepehr,[a] Heather Schmitt,[b] Janis Eells,[b] and Mahsa Ranji[a]
[a]University of Wisconsin Milwaukee, Biophotonics Lab, Department of Electrical engineering, 3200 N Cramer Street, Milwaukee, Wisconsin 53211
[b]University of Wisconsin Milwaukee, Photobiomodulation Laboratory, Department of Health Sciences, 2200 E. Kenwood Boulevard, Milwaukee, Wisconsin 53201

Abstract. Oxidative stress (OS) and mitochondrial dysfunction contribute to photoreceptor cell loss in retinal degenerative disorders. The metabolic state of the retina in a rodent model of retinitis pigmentosa (RP) was investigated using a cryo-fluorescence imaging technique. The mitochondrial metabolic coenzymes nicotinamide adenine dinucleotide (NADH) and flavin adenine dinucleotide (FAD) are autofluorescent and can be monitored without exogenous labels using optical techniques. The cryo-fluorescence redox imaging technique provides a quantitative assessment of the metabolism. More specifically, the ratio of the fluorescence intensity of these fluorophores (NADH/FAD), the NADH redox ratio (RR), is a marker of the metabolic state of the tissue. The NADH RR and retinal function were examined in an established rodent model of RP, the P23H rat compared to that of non-dystrophic Sprague-Dawley (SD) rats. The NADH RR mean values were 1.11 ± 0.03 in the SD normal and 0.841 ± 0.01 in the P23H retina, indicating increased OS in the P23H retina. Electroretinographic data revealed a significant reduction in photoreceptor function in P23H animals compared to SD nozrmal rats. Thus, cryo-fluorescence redox imaging was used as a quantitative marker of OS in eyes from transgenic rats and demonstrated that alterations in the oxidative state of eyes occur during the early stages of RP. [DOI: 10.1117/1.JBO.18.1.016004]

Keywords: optical imaging; nicotinamide adenine dinucleotide; flavin adenine dinucleotide; nicotinamide adenine dinucleotide redox ratio; oxidative stress; inherited retinal degeneration; mitochondrial dysfunction.

Paper 12431 received Jul. 8, 2012; revised manuscript received Nov. 27, 2012; accepted for publication Nov. 29, 2012; published online Jan. 4, 2013.

1 Introduction

Irreversible loss of rod photoreceptors is the outcome of abnormal physiology associated with mutated or absent gene products and leads to blindness in many retinal degenerative disorders, including retinitis pigmentosa (RP). RP is a large, genetically heterogeneous group of inherited retinal degenerations characterized by progressive and neurodegenerative photoreceptor apoptosis with subsequent degeneration of the cone photoreceptors and the retinal pigment epithelium (RPE) cells.[1,2] RP is the leading cause of inherited retinal degeneration-associated blindness in the developed world.[3] To date, 52 genes are known to be associated with all forms of RP inheritance.[4] Although the majority of RP cases are monogenic, the disease is characterized by its genetic heterogeneity and approximately 10% of the RP cases are due to defects in the rhodopsin (RHO) gene.[5] The Pro23His (P23H) RHO mutation underlies the most common form of human autosomal dominant retinitis pigmentosa (adRP).[6] The symptoms of RP are well characterized and a prominent early clinical feature of RP manifests as night blindness with peripheral visual field loss as a result of the death of rod photoreceptor cells.[7–9]

Photoreceptors are the most metabolically active cells in the body. They contain a dense concentration of mitochondria in their inner segments that provides the ATP for the energy-intensive processes of outer segment renewal and maintenance of the dark current.[7] The high metabolic demand in photoreceptors for phototransduction processes is met by mitochondrial oxidative phosphorylation (OXPHOS). The retina is also adequately supplied with glucose and oxygen by the choroidal vessels through the RPE cells. ATP is generated as a result of the synchronized activity of the tricarboxylic acid (TCA) cycle and the multi enzyme complex-electron transport chain (ETC). The coenzymes nicotinamide adenine dinucleotide (NADH)[10] and flavin adenine dinucleotide ($FADH_2$) are electron carriers in the ETC. Between 0.4–4.0% of all oxygen consumed in OXPHOS is transformed to superoxide (O_2^-) radicals[8] which are converted to H_2O_2 by Mn superoxide dismutase[9] and finally to molecular H_2O by glutathione peroxidase (GPX) or peroxiredoxin III (PRX III).[11] However, the inability of the antioxidant systems (superoxide dismutase, glutathione and thioredoxin systems) in the mitochondria to quench the increased production of reactive oxygen species[12] creates a biochemical imbalance known as oxidative stress (OS), resulting in oxidative damage to the mitochondrial proteins, lipids and DNA. This oxidative damage initiates a cascade of events resulting in mitochondrial dysfunction and cell death.[8,9,13] Considerable evidence supports a key role for mitochondrial dysfunction and oxidative damage in the pathogenesis of progressive photoreceptor cell death by apoptosis in RP both *in vitro*[14,15] and *in vivo*.[15–17] Mitochondrial dysfunction and OS have also been documented in other retinal

*Authors contributed equally.

Address all correspondence to: Mahsa Ranji, University of Wisconsin Milwaukee, Biophotonics Lab, Department of Electrical engineering, 3200 N Cramer Street, Milwaukee, Wisconsin 53211. Tel: (414) 229-5889; E-mail: ranji@uwm.edu or Janis Eells, University of Wisconsin Milwaukee, Photobiomodulation Laboratory, Department of Health Sciences, 2200 E. Kenwood Boulevard, Milwaukee, Wisconsin 53201, E-mail: jeells@uwm.edu

0091-3286/2013/$25.00 © 2013 SPIE

degenerative disorders including glaucoma, age-related macular degeneration (AMD) and diabetic retinopathy (DR), as well as numerous neurodegenerative disorders including Parkinson's disease and Alzheimer's disease.[10,18–20]

Optical fluorescence techniques have been shown to possess a high sensitivity and specificity for discriminating between diseased and nondiseased tissue. Fluorescence imaging provides specific information on tissue intrinsic fluorophores as a diagnostic tool for early detection of different diseases.[12,21–24] Although a link between oxidative stress and photoreceptor degeneration has been proposed, a direct analysis of the redox state within the mitochondrial compartment of the rodent eye has not been performed. We hypothesized that there would be a significant difference in the optical redox ratio of the dystrophic retina of the P23H rat compared to that of the nondystrophic normal rat. We tested this hypothesis using a three-dimensional (3-D) optical cryofluorescence imaging technique.

Mitochondrial metabolic coenzymes NADH and $FADH_2$ are two of the primary electron donors and acceptors in OXPHOS, respectively. NADH and FAD (the oxidized form of $FADH_2$) are autofluorescent and can be monitored without exogenous labels through the use of optical techniques. NADH is primarily fluorescent in its reduced biochemical state, whereas FAD is only fluorescent in its oxidized form. Therefore, by imaging these two coenzymes, we can probe the mitochondrial redox state of the tissue. The fluorescent signals of these intrinsic fluorophores have been used as indicators of tissue metabolism in injuries due to hypoxia,[12,22–24] ischemia,[12,23] and diabetes.[22] Our studies have demonstrated that the ratio of these fluorophores, (NADH/FAD), called the NADH redox ratio (NADH RR), acts as a quantitative marker of the mitochondrial redox and metabolic state of tissue *ex vivo*[25] and *in vivo*.[26] Although this ratio is not a direct measure of the concentrations of these fluorophores, the fluorescence intensity measured is a relative measure of their concentrations.[22]

2 Materials and Methods

We evaluated the mitochondrial redox state quantitatively in the *in situ* retina using a 3-D fluorescent optical imaging instrument called the cryoimager to detect the oxidative state of the retina in P23H transgenic (diseased) eyes as well as Sprague-Dawley (SD) normal eyes.

2.1 *Animal Preparation*

All animal experiments were approved by the Institutional Animal Care and Use Committee (IACUC) and were conducted in accordance with the The Association for Research in Vision and Ophthalmology (ARVO) statement for the use of animals in ophthalmic and vision research and with the National Institutes of Health regulations. All animals were housed and bred in an American Association for Accreditation of Laboratory Animal Care (AAALAC) approved animal facility at the University of Wisconsin-Milwaukee.

Albino SD normal and heterozygous P23H-1 transgenic rats, the offspring of P23H-1 homozygotes (Retinal Degeneration Rat Model Resource, UCSF) and SD normal albino rats (Harlan Laboratories, Madison) were fed *ad libitum* and maintained in a temperature and humidity-controlled environment under dim cyclic light, 12-h light/12-h dark cycle, with an average illuminance of 5 to 10 lux inside the cage. Once animals reached postnatal day 30 (P30), they were divided into two groups. The heterozygous P23H-1 rats were the model of retinal degeneration and SD normal albino rats were used as nondystrophic controls.

2.2 *Electroretinogram Recording*

The function of the retina was monitored using full-field flash electroretinography (HMs ERG system, Ocuscience LLC, Rolla, Missouri), which measures the electrical impulses emitted by the retina in response to flashes of light. Animals were dark adapted for 2 h prior to recording and were prepared under red dim light. Animals were anesthetized with xylazine/ketamine cocktail (100 and 5 mg/kg, respectively, ip). Pupils were dilated with 0.1% atropine and mild topical anesthesia (proparacaine 0.5%) was applied to the eyes. Animals were placed on a heating pad to maintain the body temperature at 37°C during the entire recording time. A silver-embedded nylon coated gold nylon thread electrode was placed on the corneal surface, overlaid with 21% methylcellulose and a small drop of methylcellulose was placed into the concave side of the contact lens before it was placed over the thread electrode. The corneal contact lens was adjusted so that it was centered on the retina. A stainless steel needle ground electrode was inserted on top of the head (midline). Stainless steel needle reference electrodes were inserted subcutaneously on either side of the base of the ear. Needle electrodes were secured with surgical tape. Signals obtained from the corneal surface were amplified, digitized and averaged using ERG view 2.5 software (Retvet CorpOcuscience, Rolla, Missouri). This software allows for low pass filtering of the final ERG test waveforms before they are graphed on the unit. This filter can be used to remove environmental and unit generated noise from the observed ERG. A custom designed Faraday cage was employed to block 60 Hz cycle electrical noise. The amplitudes and latencies of the a-waves (photoreceptor responses) and b-waves (bipolar cell and Muller cell responses) were stored in a Compact Flash storage card and fit to a computational model to determine transduction parameters for photoreceptor responses.

In both the normal and transgenic groups, eight eyes ($n = 8$) were used to assess the a-wave amplitude, whereas six eyes ($n = 6$) were used to assess the b-wave amplitude. To evaluate the a-wave and b-wave implicit time, four eyes ($n = 4$) in each of the normal and transgenic groups were used.

2.3 *Freezing and Embedding*

SD normal and P23H-1 transgenic rats were euthanized at P30. The eyes were enucleated and frozen rapidly in dry-ice for low temperature cryoimaging. For fluorescence imaging, the tissue was embedded in a customized black mounting medium (that is not fluorescent in the excitation wavelengths) and placed on a chilled aluminum plate to keep the tissue in place for freezing and slicing. The embedding process starts with freezing the base medium, embedding the tissue and fixing its position by adding more black medium around the tissue. After embedding, the tissue was stored in an ultralow freezer (−80°C) for subsequent imaging. The plate was then installed in the cryoimager where the surface of the black medium is parallel to a microtome. Figure 1 shows a frozen eye sample and an eye sample embedded in the customized black mounting medium. For the cryoimaging studies, a total of two groups of rats, four eyes per group were used.

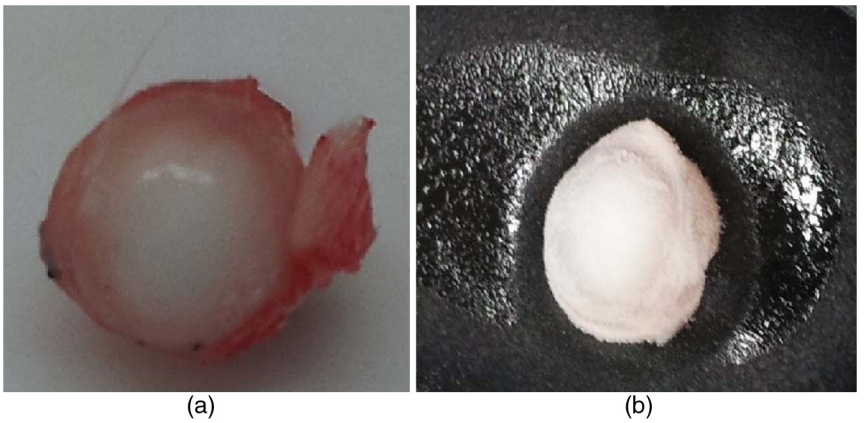

Fig. 1 (a) Frozen eye tissue (b) Embedding frozen eye in customized mounting medium.

2.4 *Imaging Calibration*

A calibration method was designed to compensate for day-to-day variation of light intensity and nonuniformity of the illumination pattern. At the beginning of each experiment and before slicing the tissue, a uniform fluorescent flat plate was placed in the same position as tissue and imaged in the NADH and FAD channels to acquire the illumination pattern. Since the fluorescence of the standard is in both the NADH and FAD channels, it also accounts for day-to-day light intensity and uniformity changes in all channels. All the images in each channel were then normalized by dividing each image to the flat plate image, captured in the same channel.

2.5 *Cryoimager*

The cryoimager, which is shown in Fig. 2 is an automated image acquisition and analysis system consisting of software and hardware designed to acquire fluorescence images of tissue sections. A motor-driven microtome sequentially sections frozen tissue at the desired slice thickness whereas filtered light from a mercury arc lamp excites up to five fluorophores in the exposed surface of the tissue block. The excitation light source is a 200 W mercury-arc lamp (white light, 200 to 800 nm) that can be filtered at any excitation and emission wavelength pairs, specifically those

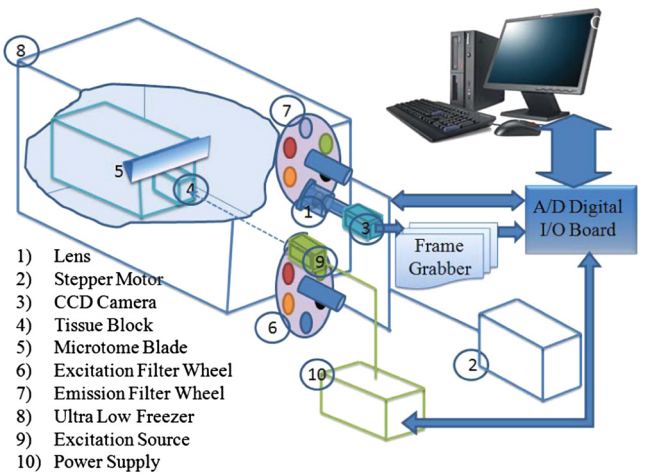

Fig. 2 Schematic of Cryoimager. This device sequentially slices the tissue, imaging the surface between each successive slice, in as many as 5 channels. The images are then displayed and saved to a computer, where they can be processed to create a 3-D rendering of the tissue.

of NADH and FAD in our studies. The excitation band pass filters used for NADH is 350 nm (80 nm bandwidth, UV Pass Blacklite, HD Dichroic, Los Angeles, California) and for FAD is 437 nm (20 nm bandwidth, 440QV21, Omega Optical, Brattleboro, Vermont) and the emission filter for NADH is 460 nm (50 nm bandwidth, D460/50M, Chroma, Bellows Falls, Vermont) and for FAD is 537 nm (50 nm bandwidth, QMAX EM 510-560, Omega Optical, Brattleboro, Vermont). Using these filters, the excitation power of NADH and FAD is 20 $\mu w/mm^2$.

At each slice, a charge coupled device (CCD) camera records fluorescence images of the tissue block in pixel dimensions of 10×10 μm^2 to be later analyzed for fluorophore distribution. The microtome is housed in a freezer unit that maintains the sample at −20°C during sample slicing and image acquisition. The resolution in the z direction of microtome slices can be as small as 5 μm. For this study, we used a resolution of 10 μm in the z direction, which resulted in ~500 z-slices per eye.[24,27]

2.6 *Image Processing*

NADH and FAD autofluorescence images (containing 500 slices per eye) from each group of eyes were processed using MATLAB. Composite images were created using all the image slices for each eye, for both NADH and FAD signals. The ratio of NADH and FAD, was calculated voxel by voxel, using MATLAB, according to Eq. (1):

$$\text{NADH Redox Ratio} = \text{NADH RR} = \text{NADH/FAD}. \quad (1)$$

The two-dimensional representation of each eye was then calculated using the maximum intensities along the z axis of the NADH redox 3-D volume (maximum projection). In the maximum projection method, first a full 3-D volume of images was obtained, including RR, and then the maximum projection on the volumetric data was performed and the histograms were plotted for this maximum projection. The maximum projection is used since the entirety of the anatomy has a significant contribution in this representation. A histogram of the max projection of RR values in each group was created, and the mean (or first moment) of this histogram was calculated according to Eq. (2):

$$\text{Mean} = \frac{1}{N_x \times N_y} \sum_{i=1}^{N_x} \sum_{j=1}^{N_y} \text{Eye MaxPro}(i, j), \quad (2)$$

where N_x and N_y are the number of pixels in the x and y directions and the pixel size in x and y is 10 and 10 μm. The

previously mentioned histograms were calculated for quantitative comparison between normal and diseased groups.

2.7 *Statistical Evaluation of Data*

Data are presented as mean ± SEM. A mixed model 2×6 ANOVA with animal group (P23H versus SD) as the between-subjects factor and flash intensities of the scotopic intensity series as the within-subjects factor was used to analyze ERG data. A Greenhouse-Geisser correction (a-wave = .500; b-wave = .460) was performed as the assumption of sphericity was violated for the a-wave ($X^2 = 31.140$, $p = .006$) and b-wave ($X^2 = 28.381$, $p = .016$) data. An unpaired Student's t-test was used for comparing mean values of NADH redox ratio and a-wave and b-wave implicit times at 100 mcd.s/m^2. Statistical analysis was performed using SPSS 19.0 (SPSS Inc, Chicago, Illinois) and GraphPad Prism 4.0 (GraphPad, La Jolla, California). The level of significance for all statistical tests was set at 0.05.

3 Results

In the present study, we used the cryo-fluorescence redox imaging method to probe the retinal mitochondrial redox state. The method was performed on P23H transgenic eyes and SD normal eyes at postnatal day 30, to determine the effect of disease on the NADH RR. This method detects changes in the oxidation state of the mitochondrial respiratory chain. Thus, NADH RR can be used as a quantitative marker to evaluate the OS in diseased and normal eye tissue.

A representative 3-D rendering of NADH redox images from a rat eye sample is shown in Fig. 3 with a volume rendering that includes the optic nerve of the eye.

NADH, FAD, and NADH RR images have been used to show the changes in the oxidation state of the mitochondria due to an increase in OS at the presence of the disease. As can be seen from Fig. 4, in the presence of an excess amount of OS in transgenic eyes, we expect to have lower concentrations of NADH and a higher concentration of FAD which causes the NADH RR to be lower (more oxidized) in eyes from transgenic rats compared to the eyes from SD normal rats (more reduced).

To have a better comparison of the intensity of the redox ratio image, which is a marker of the oxidation state of the mitochondria in normal and diseased groups, the histograms of RR for the

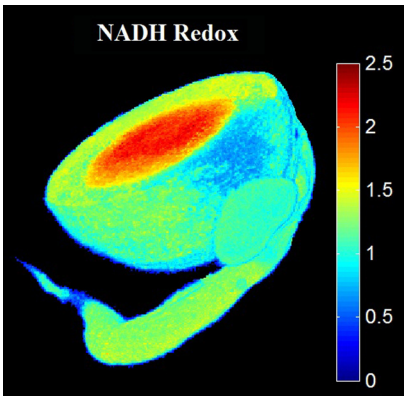

Fig. 3 Volume rendering of NADH redox of a representative eye to show the capability of the cryoimager to perform 3-D imaging on intact tissue.

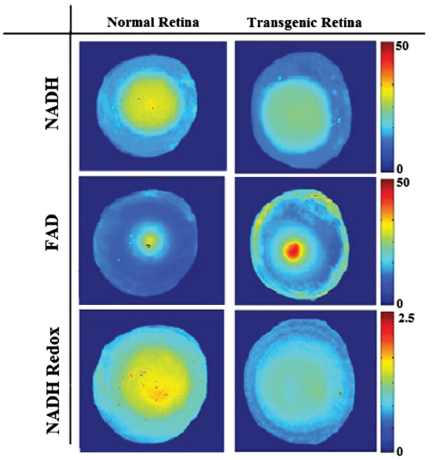

Fig. 4 Representative max projected NADH, FAD and NADH RR images for a representative eye in transgenic and SD normal groups. The images show a significant decrease in the mean NADH RR of eyes from diseased versus SD normal group.

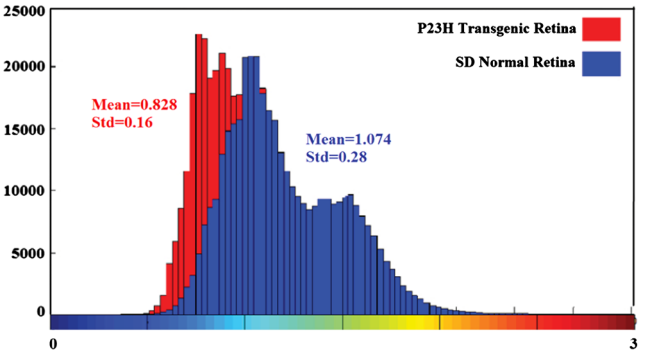

Fig. 5 A representative histogram for eyes from normal and diseased groups comparing NADH RR intensity between P23H transgenic retina versus SD normal retina. Oxidative stress causes more oxidation in the NADH redox histogram.

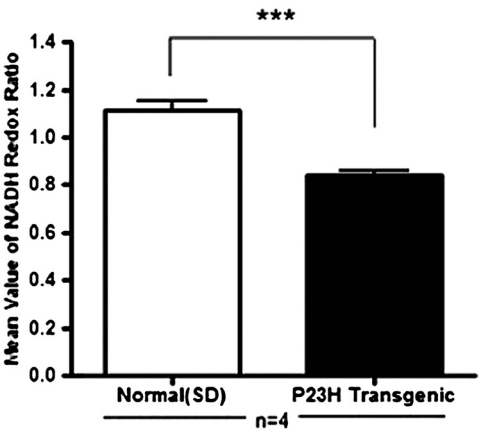

Fig. 6 Bar graph plot comparing the mean values of the histograms of max projected images from SD normal and P23H transgenic rat eyes. The results show a significant difference between normal and diseased eyes (***$P < .001$). Error bars: SEM; P values were obtained from an unpaired Student's t-test.

two sets of eyes in Fig. 4 were plotted. These histograms in Fig. 5 confirm the results from Fig. 4, which in the diseased group the NADH RR indicates a more oxidized biochemical state with a mean value of 0.821 compared with a higher mean value of 1.079 in SD normal eyes. There was a blue shift in histograms from P23H transgenic eye versus the normal eye and the NADH redox histogram shows a 24% oxidation in the respiratory chain in this group.

To show the statistical significance of our results, four eyes in each group of SD normal and P23H transgenic eyes were tested and the mean values of the histograms of max projected images were compared, as can be seen in Fig. 6. The results show a significant difference ($p < .001$) between the mean NADH RR of P23H transgenic eyes versus the SD normal eyes, confirming the efficacy of using the NADH RR as a quantitative marker of OS.

Table 1 shows the mean values of the NADH RR for SD normal and P23H transgenic rat eyes. The mean values were significantly lower in transgenic eyes when compared to normal eyes. Therefore, the decreased NADH RR in transgenic eyes is attributable to the increase in OS of the mitochondria.

Figure 7 shows a comparison of the functional response of the retina in the nondystrophic SD rats compared to P23H RP rats. The a-wave reflects the functional activity of the photoreceptor cells. As shown in Fig. 7(a), the photoreceptor response in the SD retina rises linearly from 144.6 ± 12.9 μV to 426.2 ± 20.1 μV compared with a significantly attenuated increase from 44.7 ± 4.2 μV to 115.5 ± 20.1 μV measured in the P23H retina. The response of the bipolar and Muller cells of the retina, reflected in the b-wave, is also attenuated in the P23H rat as shown in Fig. 7(b).

Table 2 compares the functional response of the retina in SD normal rats versus P23H RP rats for the flash intensity of 1000 mcd.s/m^2. P23H transgene caused a significant decrease in both a-wave and b-wave amplitudes compared to the normal SD controls as can be seen from Table 2.

The implicit time reflects the peak latencies in a-wave and b-wave amplitudes and Fig. 8 compares a-wave and b-wave implicit times assessed at 100 mcd.s/m^2. We observed a significant ($p < .01$) delay in both a- and b- wave implicit times in P23H retina compared to SD rats. The delay and deviations of the implicit time topography in RP when compared to normal subjects is a characteristic diagnostic feature of this disease.[3,7]

Table 3 compares a-wave and b- wave implicit times assessed at 100 mcd.s/m^2. There is a delay in both a- and b- wave implicit times in P23H retina compared to SD rats as can be seen from the table.

Table 1 Summary of cryoimaging results on SD normal and P23H transgenic eyes.

Rat models	n	Mean value of NADH RR (mean ± SEM)
SD Normal	4	1.11 ± 0.03^a
P23H Transgenic	4	0.841 ± 0.01

[a]$P < .001$

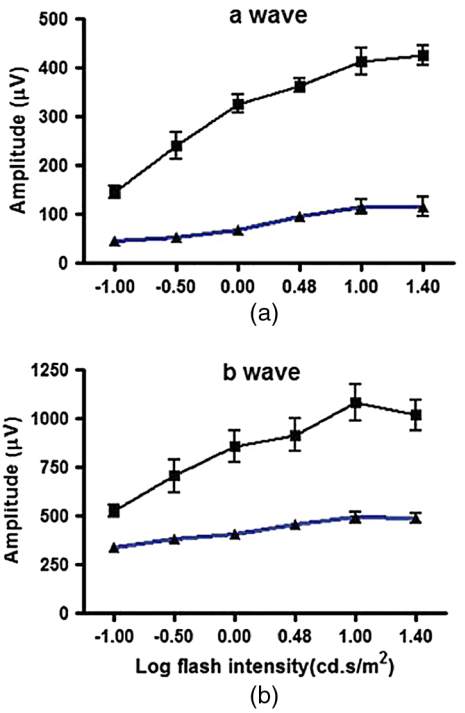

Fig. 7 (a) The mean a-wave amplitude assessed by the scotopic intensity series protocol comparing P23H transgenic (▲; $n = 8$) and SD normal control (■; $n = 8$) groups (b) the mean b-wave amplitude comparing P23H transgenic (▲; $n = 6$) and SD normal control (■; $n = 6$) groups. P23H transgene caused a significant decrease in both a-wave [$F_{(1,14)} = 161.0$, $p < .001$; Fig. 7(a)] and b-wave [$F_{(1,10)} = 35.4$, $p < .001$; Fig. 7(b)] amplitudes at all flash intensities compared to the normal SD controls. Error bars: SEM.

Table 2 Summary of ERG results on SD normal and P23H transgenic eyes.

Mouse models	n	a-wave amplitude (μv) (1000 mcd.s/m^2)	n	b-wave amplitude (μv) (1000 mcd.s/m^2)
SD Normal	8	326.6 ± 19.2^a	6	856.1 ± 82.6^a
P23H transgenic	8	68.2 ± 6.0	6	406.5 ± 15.2

[a]$P < .001$

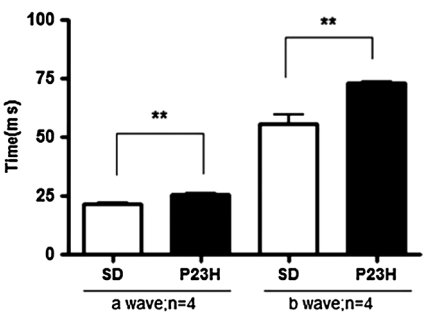

Fig. 8 The figure shows the a-wave implicit time as well as b-wave implicit time assessed at 100 mcd.s/m^2 in SD and P23H rats at P30. The implicit times reflecting peak latencies of a- and b- waves were significantly ($**P < .01$) different between P23H transgenic and normal SD retina. Error bars: SEM; p values were obtained from an unpaired Student's t-test.

Table 3 Summary of implicit time assessing results on SD normal and P23H transgenic eyes.

Mouse models	*n*	a-Wave implicit time (ms)	b-Wave implicit time (ms)
SD Normal	4	21.4 ± 0.4^a	55.6 ± 3.8^a
P23H Transgenic	4	25.5 ± 0.6	73.0 ± 0.5

[a]$P < .01$

4 Discussion and Conclusion

The retina is particularly vulnerable to oxidative damage since it is one of the highest oxygen consuming tissues of the body and about 90% of tissue oxygen is metabolized within the mitochondria.[28] Markers of oxidative damage to proteins, lipids and DNA have been detected in cone photoreceptors in the transgenic pig model of RP. This suggests that as the rod photoreceptors degenerate, there is a reduction in oxygen consumption in the outer retina. Decreased oxygen consumption results in a subsequent increase in oxidative stress, which causes hyperoxia in the photoreceptor layer leading to cone loss.[28,29] Understanding the biochemical mechanisms involved in cone photoreceptor degeneration is important since cone loss is the major reason for visual loss in RP. In addition, the method presented here examines mitochondrial oxidative metabolism, which, for the above reason, represents an early marker of RP disease progression.

The P23H RHO transgenic rat is a widely used and well characterized rodent model of RP.[30] In this rodent model of RP, photoreceptor cells begin to die at P16, peaking at P25 and declining to low adult rates.[28] At P30, when these animals were evaluated, the numbers of photoreceptor cells in the outer nuclear layer of the retina is half of that measured in the nondystrophic SD rat.[30] The electroretinogram is a functional measure of outer retinal activity in response to light.[30] As illustrated in Fig. 7, both the a-wave (photoreceptor response) and b-wave (bipolar cell and Muller glial cell response) are significantly attenuated in the P23H retina compared with the nondystrophic SD retina consistent with the pathology of the disease. The function of the surviving photoreceptors is attenuated as indicated by the increase in the latency of the response. Our observations of increased oxidative stress in the P23H retina compared with the SD retina are consistent with the pathogenesis of RP and the observed attenuation of retinal function. Retinal metabolic imaging has the potential to be a valuable diagnostic tool for the assessment of the progression of RP or the efficacy of therapeutic interventions.

In the presence of hyperoxia, as seen in RP and other inherited retinal degenerations, mitochondrial redox fluorophores accumulate in their oxidized forms (NAD and FAD). This results in the NADH RR showing a significant decrease in the degenerating eye as compared to the SD normal as shown in Fig. 6. The difference in the mean values of the two histograms in Fig. 5 suggests that OS caused by the disease in transgenic eyes is the reason for a shift in metabolic levels of the cells in the eye tissue and causes the mitochondrial respiratory chain to be more oxidized. The 24% oxidation in the NADH RR that we observed in the retina of P23H transgenic rat model suggests that substantial mitochondrial OS is a significant early cellular event in RP. The significant difference in the mean NADH RR of eyes from transgenic rats compared with their appropriate controls (SD normal eyes) suggests that the sensitivity of RR can be used as a marker of retinal OS. This sensitivity has been shown in our previous studies, where RR has also been used as a marker of OS in DR.[31]

Most of the existing retinal imaging modalities, such as fundus photography,[32,33] scanning laser ophthalmoscope (SLO),[34] and optical coherence tomography (OCT)[35–38] are based on the back-reflected light from the retinal tissues to provide structural information. Recent technologies, such as optical absorption imaging, on the other hand, are based on the absorption properties to provide functional information such as retinal vessel oxygenation.[39,40] Mapping the retinal vessel oxygenation and imaging the retinal vasculature is indicative of the early diagnosis of DR, characterized by retinal blood vessel malfunctions. Photoacoustic microscopy (PAM) is another optical-absorption based microscopic imaging modality that detects laser-induced ultrasonic waves as a result of optical absorption in tissue.[41–43] Abnormalities in retinal oxygenation lead to acute retinal artery embolic disease and retinal vein occlusion. Multiwavelength reflectance spectrophotometry measures oxygen saturation of blood,[44–47] and phosphorescence lifetime imaging measures intravascular oxygen tension.[47–50] Magnetic resonance imaging (MRI)[51,52] provides an indirect measure of retinal tissue oxygen tension, with limited resolution compared with optical techniques.[53]

Fluorescence redox imaging, however, provides mitochondrial dysfunction status related to retinal OS. The redox imaging technology has considerable clinical potential in retinal diseases in which mitochondrial dysfunction is an early feature including DR, macular degeneration and RP.[31–34] Early diagnosis of mitochondrial dysfunction in retinal disease would facilitate earlier therapeutic intervention and better treatment outcome.

Our studies suggest a correlation between the disruption of retinal function in RP and mitochondrial OS. OS and mitochondrial dysfunction has been shown to lead to apoptotic cell death early in the pathology of many retinal diseases.[54–59] Thus, the measurement of mitochondrial metabolic activity has considerable potential as an early clinical indicator of retinal dysfunction and disease. Flavoprotein autofluorescence has been shown to be a reliable indicator of mitochondrial dysfunction experimentally[60] and clinically[12,61] in heart and brain tissue. Recent studies have provided clinical evidence that flavoprotein autofluorescence is an early indicator of metabolic dysfunction in retinal disease.[62–64] To measure retinal flavoprotein autofluorescence these investigators employed a fundus camera modified with narrow-band excitation and emission filters, a high-sensitivity EMCCD camera and attached computers with customized software.[62–64] Using this methodology they have documented FAD autofluorescence and early metabolic dysfunction in humans with diabetes and pseudotumor cerebri.[62–64] Our methodology measures both NADH and FAD fluorophores and allows us to calculate a redox ratio, which is a diagnostic marker independent of the number of mitochondria. Although our present research was conducted *in vitro*, we plan on extending our approach to *in vivo* measurements of redox ratio by implementing micron resolution fiber optic probes to be inserted to the back of the eye for redox ratio measurements over time. Our redox ratio measurement has the advantage of evaluating the mitochondrial bioenergetics and metabolic state of retinal tissue *in vivo* independent of various factors such as absorption by other proteins, scattering effects, and changing mitochondrial protein concentration.[12] Measuring the metabolic rate of oxygen

consumption in the retina *in vivo*, is valuable in diagnosis of diseases affecting the retina, including AMD, DR, glaucoma and retinopathy of prematurity.[65] The redox ratio can be used as an indicator of retinal tissue metabolism, specifically, impairment of retinal function due to retinal oxygen disruption, *in vivo*.

Our results demonstrate the quantitative capability of an optical cryoimaging technique to measure the tissue mitochondrial redox state in the normal and diseased rat retina. This direct analysis of the cellular metabolic state within the mitochondrial compartment of the retina in a transgenic rat model of RP has not previously been reported. Furthermore, the studies presented here set the stage for future studies, using *ex vivo* and *in vivo* fluorescence imaging of mitochondrial redox states of retina to characterize disease progression in retinal dystrophies and to evaluate mitochondria targeted drug regimens that diminish OS.

Acknowledgments

M.R. was supported, in part, by a UWM RGI 6 award and a NIH/CTSI K12 (8KL2TR000056 and 8UL1TR000055) award. We acknowledge the support of a Foundation Fighting Blindness Individual Investigator Award (TA-NP-0709-0465-UWI), and an Award from the International Retinal Research Foundation (J.T.E.). S.G. was funded, in part, by College of Health Sciences Research Grant Award, University of Wisconsin, Milwaukee. We acknowledge the assistance of Dr. Wendy Huddleston in statistics and data analysis.

References

1. D. Besch et al., "Inherited multifocal RPE-diseases: mechanisms for local dysfunction in global retinoid cycle gene defects," *Vision Res.* **43**(28), 3095–3108 (2003).
2. J. Sancho-Pelluz et al., "Photoreceptor cell death mechanisms in inherited retinal degeneration," *Mol. Neurobiol.* **38**(3), 253–269 (2008).
3. D. T. Hartong, E. L. Berson, and T. P. Dryja, "Retinitis pigmentosa," *Lancet* **368**(9549), 1795–1809 (2006).
4. K. Neveling et al., "Next-generation genetic testing for retinitis pigmentosa," *Hum. Mutat.* **33**(6), 963–972 (2012).
5. T. P. Dryja et al., "Mutations within the rhodopsin gene in patients with autosomal dominant retinitis pigmentosa," *N. Engl. J. Med.* **323**(19), 1302–1307 (1990).
6. M. Haeri and B. E. Knox, "Rhodopsin mutant P23H destabilizes rod photoreceptor disk membranes," *PLoS One* **7**(1), e30101 (2012).
7. A. N. Bramall et al., "The genomic, biochemical, and cellular responses of the retina in inherited photoreceptor degenerations and prospects for the treatment of these disorders," *Annu. Rev. Neurosci.* **33**, 441–472 (2010).
8. M. K. Shigenaga, T. M. Hagen, and B. N. Ames, "Oxidative damage and mitochondrial decay in aging," *Proc. Natl. Acad. Sci. U. S. A.* **91**(23), 10771–10778 (1994).
9. D. C. Wallace, "A mitochondrial paradigm of metabolic and degenerative diseases, aging, and cancer: a dawn for evolutionary medicine," *Annu. Rev. Genet.* **39**(1), 359–407 (2005).
10. P. P. Karunadharma et al., "Mitochondrial DNA damage as a potential mechanism for age-related macular degeneration," *Invest. Ophthalmol. Vis. Sci.* **51**(11), 5470–5479 (2010).
11. K. Green, M. D. Brand, and M. P. Murphy, "Prevention of mitochondrial oxidative damage as a therapeutic strategy in diabetes," *Diabetes* **53**(Suppl 1), S110–S118 (2004).
12. M. Ranji et al., "Fluorescence spectroscopy and imaging of myocardial apoptosis," *J. Biomed. Opt.* **11**(6), 064036 (2006).
13. D. Vlachantoni et al., "Evidence of severe mitochondrial oxidative stress and a protective effect of low oxygen in mouse models of inherited photoreceptor degeneration," *Hum. Mol. Genet.* **20**(2), 322–335 (2011).
14. N. Sanvicens et al., "Oxidative stress-induced apoptosis in retinal photoreceptor cells is mediated by calpains and caspases and blocked by the oxygen radical scavenger CR-6," *J. Biol. Chem.* **279**(38), 39268–39278 (2004).
15. M. M. Sanz et al., "Significant photoreceptor rescue by treatment with a combination of antioxidants in an animal model for retinal degeneration," *Neuroscience* **145**(3), 1120–1129 (2007).
16. M. Donovan, R. J. Carmody, and T. G. Cotter, "Light-induced photoreceptor apoptosis *in vivo* requires neuronal nitric-oxide synthase and guanylate cyclase activity and is caspase-3-independent," *J. Biol. Chem.* **276**(25), 23000–23008 (2001).
17. H. Yamada et al., "Fibroblast growth factor-2 decreases hyperoxia-induced photoreceptor cell death in mice," *Am. J. Pathol.* **159**(3), 1113–1120 (2001).
18. G. Y. Kong et al., "Mitochondrial dysfunction and glaucoma," *J. Glaucoma.* **18**(2), 93–100 (2009).
19. S. R. Pieczenik and J. Neustadt, "Mitochondrial dysfunction and molecular pathways of disease," *Exp. Mol. Pathol.* **83**(1), 84–92 (2007).
20. M. T. Lin and M. F. Beal, "Mitochondrial dysfunction and oxidative stress in neurodegenerative diseases," *Nature* **443**(7113), 787–795 (2006).
21. N. Ramanujam et al., "Low temperature fluorescence imaging of freeze-trapped human cervical tissues," *Opt. Express* **8**(6), 335–343 (2001).
22. S. Maleki et al., "Mitochondrial redox studies of oxidative stress in kidneys from diabetic mice," *Biomed. Opt. Express* **3**(2), 273–281 (2012).
23. M. Ranji et al., "Quantifying acute myocardial injury using ratiometric fluorometry," *IEEE Trans. Biomed. Eng.* **56**(5), 1556–1563 (2009).
24. R. Sepehr et al., "Optical imaging of tissue mitochondrial redox state in intact rat lungs in two models of pulmonary oxidative stress," *J. Biomed. Opt.* **17**(4), 046010 (2012).
25. M. Ranji et al., "Simultaneous fluorometry and phosphorometry of Langendorff perfused rat heart: *ex vivo* animal studies," *Opt. Lett.* **31**(20), 2995–2997 (2006).
26. M. Matsubara et al., "*In vivo* fluorometric assessment of cyclosporine on mitochondrial function during myocardial ischemia and reperfusion," *Ann. Thorac. Surg.* **89**(5), 1532–1537 (2010).
27. S. L. Bernard et al., "High spatial resolution measurements of organ blood flow in small laboratory animals," *Am. J. Physiol. Heart Circ. Physiol.* **279**(5), H2043–H2052 (2000).
28. D. Y. Yu and S. J. Cringle, "Oxygen distribution and consumption within the retina in vascularised and avascular retinas and in animal models of retinal disease," *Prog. Retin. Eye Res.* **20**(2), 175–208 (2001).
29. D. S. Cassarino et al., "Cyclosporin A increases resting mitochondrial membrane potential in SY5Y cells and reverses the depressed mitochondrial membrane potential of Alzheimer's disease cybrids," *Biochem. Biophys. Res. Commun.* **248**(1), 168–173 (1998).
30. S. Machida et al., "P23H rhodopsin transgenic rat: correlation of retinal function with histopathology," *Invest. Ophthalmol. Vis. Sci.* **41**(10), 3200–3209 (2000).
31. Z. Ghanian et al., "Optical imaging of oxidative stress in diabetic retinopathy," in *Biomedical Engineering Society*, Atlanta (2012).
32. F. C. Delori et al., "Monochromatic ophthalmoscopy and fundus photography. The normal fundus," *Arch. Ophthalmol.* **95**(5), 861–868 (1977).
33. G. A. Williams et al., "Single-field fundus photography for diabetic retinopathy screening: a report by the American Academy of Ophthalmology," *Ophthalmology* **111**(5), 1055–1062 (2004).
34. R. H. Webb and G. W. Hughes, "Scanning laser ophthalmoscope," *IEEE Trans. Biomed. Eng.* **28**(7), 488–492 (1981).
35. D. Huang et al., "Optical coherence tomography," *Science* **254**(5035), 1178–1181 (1991).
36. M. Wojtkowski et al., "*In vivo* human retinal imaging by Fourier domain optical coherence tomography," *J. Biomed. Opt.* **7**(3), 457–463 (2002).
37. N. Nassif et al., "*In vivo* high-resolution video-rate spectral-domain optical coherence tomography of the human retina and optic nerve," *Opt. Express* **12**(3), 367–376 (2004).
38. M. Ruggeri et al., "*In vivo* three-dimensional high-resolution imaging of rodent retina with spectral-domain optical coherence tomography," *Invest. Ophthalmol. Vis. Sci.* **48**(4), 1808–1814 (2007).

39. A. Harris et al., "A review of methods for human retinal oximetry," *Ophthalmic Surg. Laser. Imag.* **34**(2), 152–164 (2003).
40. M. Hammer et al., "Light paths in retinal vessel oxymetry," *IEEE Trans. Biomed. Eng.* **48**(5), 592–598 (2001).
41. H. F. Zhang, K. Maslov, and L. V. Wang, "*In vivo* imaging of subcutaneous structures using functional photoacoustic microscopy," *Nat. Protoc.* **2**(4), 797–804 (2007).
42. H. F. Zhang et al., "Functional photoacoustic microscopy for high-resolution and noninvasive *in vivo* imaging," *Nat. Biotechnol.* **24**(7), 848–851 (2006).
43. K. Maslov et al., "Optical-resolution photoacoustic microscopy for *in vivo* imaging of single capillaries," *Opt. Lett.* **33**(9), 929–931 (2008).
44. M. H. Smith et al., "Oxygen saturation measurements of blood in retinal vessels during blood loss," *J. Biomed. Opt.* **3**(3), 296–303 (1998).
45. D. Schweitzer et al., "A new method for the measurement of oxygen saturation at the human ocular fundus," *Int. Ophthalmol.* **23**(4–6), 347–353 (2001).
46. M. Hammer and D. Schweitzer, "Quantitative reflection spectroscopy at the human ocular fundus," *Phys. Med. Biol.* **47**(2), 179–191 (2002).
47. K. R. Denninghoff et al., "Retinal venous oxygen saturation and cardiac output during controlled hemorrhage and resuscitation," *J. Appl. Physiol.* **94**(3), 891–896 (2003).
48. R. D. Shonat et al., "Oxygen distribution in the retinal and choroidal vessels of the cat as measured by a new phosphorescence imaging method," *Appl. Opt.* **31**(19), 3711–3718 (1992).
49. R. D. Shonat and A. C. Kight, "Oxygen tension imaging in the mouse retina," *Ann. Biomed. Eng.* **31**(9), 1084–1096 (2003).
50. P. W. Ferrez et al., "Effect of visual stimulation on blood oxygenation in the optic nerve head of miniature pigs: a pilot study," *Klin. Monbl. Augenheilkd.* **221**(5), 364–366 (2004).
51. Y. Ito and B. A. Berkowitz, "MR studies of retinal oxygenation," *Vision Res.* **41**(10–11), 1307–1311 (2001).
52. R. Roberts et al., "Spatial pattern and temporal evolution of retinal oxygenation response in oxygen-induced retinopathy," *Invest. Ophthalmol. Vis. Sci.* **44**(12), 5315–5320 (2003).
53. N. D. Wangsa-Wirawan and R. A. Linsenmeier, "Retinal oxygen: fundamental and clinical aspects," *Arch. Ophthalmol.* **121**(4), 547–557 (2003).
54. M. Shahidi et al., "Three-dimensional mapping of chorioretinal vascular oxygen tension in the rat," *Invest. Ophthalmol. Vis. Sci.* **50**(2), 820–825 (2009).
55. A. Shakoor et al., "Chorioretinal vascular oxygen tensiochanges in response to light flicker," *Invest. Ophthalmol. Vis. Sci.* **47**(11), 4962–4965 (2006).
56. J. L. Dunaief et al., "The role of apoptosis in age-related macular degeneration," *Arch. Ophthalmol.* **120**(11), 1435–1442 (2002).
57. F. Podesta et al., "Bax is increased in the retina of diabetic subjects and is associated with pericyte apoptosis *in vivo* and *in vitro*," *Am. J. Pathol.* **156**(3), 1025–1032 (2000).
58. L. A. Kerrigan et al., "TUNEL-positive ganglion cells in human primary open-angle glaucoma," *Arch. Ophthalmol.* **115**(8), 1031–1035 (1997).
59. Y. Du, C. M. Miller, and T. S. Kern, "Hyperglycemia increases mitochondrial superoxide in retina and retinal cells," *Free Radic. Biol. Med.* **35**(11), 1491–1499 (2003).
60. A. Kindzelskii and H. R. Petty, "Fluorescence spectroscopic detection of mitochondrial flavoprotein redox oscillations and transient reduction of the NADPH oxidase-associated flavoprotein in leukocytes," *Eur. Biophys. J.* **33**(4), 291–299 (2004).
61. K. C. Reinert et al., "Flavoprotein autofluorescence imaging of neuronal activation in the cerebellar cortex *in vivo*," *J. Neurophysiol.* **92**(1), 199–211 (2004).
62. V. M. Elner et al., "Flavoprotein autofluorescence detection of early ocular dysfunction," *Arch. Ophthalmol.* **126**(2), 259–260 (2008).
63. M. G. Field et al., "Rapid, noninvasive detection of diabetes-induced retinal metabolic stress," *Arch. Ophthalmol.* **126**(7), 934–938 (2008).
64. S. G. Elner et al., "Retinal flavoprotein autofluorescence as a measure of retinal health," *Trans. Am. Ophthalmol. Soc.* **106**, 215–222 (2008).
65. T. Liu et al., "Combined photoacoustic microscopy and optical coherence tomography can measure metabolic rate of oxygen," *Biomed. Opt. Express* **2**(5), 1359–1365 (2011).